Available online at www.sciencedirect.com
SCIENCE DIRECT®
Journal of Computational Physics 213 (2006) 214–238
JOURNAL OF COMPUTATIONAL PHYSICS
www.elsevier.com/locate/jcp

Simulation of visible and ultra-violet group-III nitride light emitting diodes

K.A. Bulashevich [a,c], V.F. Mymrin [a], S.Yu. Karpov [a,b,*], I.A. Zhmakin [a,c], A.I. Zhmakin [a,d]

[a] *Soft-Impact, Ltd., Device Modeling Department, P.O. Box 83, 27 Engels av., St. Petersburg 194156, Russia*
[b] *Semiconductor Technology Research, Inc., P.O. Box 70604, Richmond, VA 23255-0604, USA*
[c] *A.F. Ioffe Physical Technical Institute, RAS, 26 Polytechnicheskaya str., St. Petersburg 194021, Russia*
[d] *St. Petersburg Branch of Joint Supercomputer Centre, RAS, 26 Polytechnicheskaya str., St. Petersburg 194021, Russia*

Received 7 April 2005; received in revised form 9 August 2005; accepted 10 August 2005
Available online 21 September 2005

Abstract

One-dimensional drift-diffusion model accounting for the unique properties of group-III nitrides is employed to simulate the carrier transport and radiative/non-radiative recombination of electrons and holes in light emitting diode heterostructures. Mixed finite-element method is used for numerical implementation of the model. The emission spectra are computed via the self-consistent solution of the Schrödinger–Poisson equations with account of complex valence band structure of nitride materials. Simulations of a number of single- and multiple-quantum well blue and ultraviolet light emitting diodes are presented and compared with available observations. Specific features of the III-nitride LED operation are considered in terms of modelling. Applicability of the drift-diffusion model to analysis of III-nitride LEDs is proved and still open questions are discussed.
© 2005 Elsevier Inc. All rights reserved.

PACS: 02.70.Dh; 77.65.Ly; 78.60.Fi; 85.60.Bt; 85.60.Jb

Keywords: Light emitting diode; Group-III nitrides; Drift-diffusion model; Simulation; Finite element methods

1. Introduction

Due to direct bandgaps varying in the range of 0.7–6.2 eV, group-III nitrides – AlN, GaN, and InN – and their ternary alloys have recently become basic materials for visible and ultra-violet (UV) light emitting devices [1]. The fabrication technology and engineering of these semiconductor devices, however, have currently leaved far behind a detailed understanding of mechanisms involved in their operation. This is largely because of non-ordinary properties of nitride semiconductors, like a spontaneous electric polarization, a strong piezoeffect, an extremely

* Corresponding author. Tel.: +7 812 554 4570; fax: +7 812 326 6194.
E-mail addresses: karpov@semitech.us, karpov@softimpact.ru (S.Yu. Karpov).

0021-9991/$ - see front matter © 2005 Elsevier Inc. All rights reserved.
doi:10.1016/j.jcp.2005.08.011

low acceptor activation efficiency, and a high dislocation density inherent in epitaxial materials [2]. In particular, huge polarization-induced charges accumulated at abrupt interfaces of a device heterostructure affect dramatically its band diagram. A poor acceptor activation requires special approaches to attain a satisfactory efficiency of carrier injection into the active region of a light emitting diode (LED) or a laser diode (LD). All this, in combination with a complex multi-layer heterostructure and carrier degeneration typical of most LEDs and LDs, hampers an intuitive bandgap engineering of the devices, normally based on analogies with conventional III–V compounds. Here, numerical simulation may provide a deeper insight into physical mechanisms underlying the device operation and support optimization of its heterostructure.

A global simulation of a III-nitride LED requires to treat consistently a number of issues, including (i) non-equilibrium carrier injection into the active region, electron and hole radiative/non-radiative recombination and light emission, (ii) current spreading in an LED dice with a complex contact configuration [3], (iii) light extraction from the dice, (iv) heat removal from the LED heterostructure, and (v) some reliability aspects [4]. This paper deals with the first of the above problems.

An earlier attempt of 1D-modelling of the band diagram and carrier injection in a blue InGaN/AlGaN LED has been reported in [5]. The authors referred to an LED structure fabricated by Nakamura and co-authors [6] where an $In_{0.06}Ga_{0.94}N$ active region was thick enough to provide a complete strain relaxation via generation of mismatch dislocations. The drift-diffusion (DD) model used in [5] was specially adapted to account for such specific features of wide-bandgap materials as a large range of variation of the majority/minority carrier concentration and high potential barriers formed at the structure interfaces due to a large difference in the bandgaps of neighboring materials. As a principal feature of nitride semiconductors, strong spontaneous and piezo-polarization, had not been recognized at that time, it was not considered in [5]. More accurate 2D- and 3D-simulations of blue InGaN/GaN LDs and AlGaN/GaN UV LEDs have been recently reported in [7,8]. In this studies, the APSYS and LASTIP packages by Crosslight Software were employed where the DD transport equations combined with the Shokley–Read non-radiative recombination model had been implemented. The simulations have revealed a huge effect of the built-in polarization fields on the band diagrams of the devices and on the rate of electron and hole radiative recombination in a quantum-well (QW) active region.

Despite the demonstrated capabilities of simulations to predict general trends in III-nitride operation, many questions still remain open. First, visible III-nitride LEDs normally contain a single-quantum-well (SQW) or a multiple-quantum-well (MQW) InGaN active region grown on GaN. As these materials have a large, $\sim$11%, lattice constant mismatch, the QWs cannot be obtained thick enough without generation of interface defects. Therefore, the thickness of an InGaN QW ranges normally between 1 and 4 nm. The space-charge regions formed in nitride LEDs are typically as wide as a few tens of nanometers. Since both the QW thickness and the space-charge region width are comparable with the mean free path of electrons and holes, the applicability of the DD model for simulating III-nitride LED heterostructures is not evident and requires a special justification. Second, it has been recently found that a distributed space charge can be formed in a graded-composition nitride alloy due to polarization effects [9]. Actually, such a space charge may be regarded as a result of additional doping of a heterostructure. However, a built-in pulling field arises also in a graded-composition layer, which may favor or hinder the carrier injection. Thus, the total effect of the graded-composition layers on the LED operation is not yet understood in detail and requires a special investigation. Third, a high dislocation density of $\sim 10^8$–10^{10} cm^{-2} is typically observed in III-nitride epitaxial layers grown on either sapphire or silicon carbide substrates. The dislocations serve as non-radiative recombination centers considerably lowering the internal quantum efficiency (IQE) of devices (see e.g. [10] and references therein). At the moment, the dislocation impact on the LED efficiency and other characteristics is not examined in detail. And, the question that is still obscure concerns the role of a tunnelling current frequently observed in InGaN blue and, especially, green LEDs (see for instance [11]).

In this paper, we report on the use of one-dimensional DD model for simulating the carrier transport and light emission in III-nitride LED heterostructures, with the focus on the model applicability and its validation. The problems of numerical solution of the DD equations, originated from specific features of III-nitride semiconductors, are discussed. Comparison with experimental data reported for a number of SQW and MQW blue and UV LED structures is done to validate the model.

There are additional reasons stimulating our interest to a 1D-model of III-nitride LEDs. From the practical point of view, the most critical characteristic of any simulation approach is the time necessary to get an

engineering guideline for device structure design or/and its optimization. Being capable of predicting the principal trends in the device operation, a 1D-model may have advantages over more accurate 2D- and 3D-models due to a shorter response time and an easier implementation of novel physical mechanisms. This is especially evident for III-nitrides having many materials properties known with an insufficient accuracy, so that the simulation predictability is no longer limited by the dimensionality of the approach.

The paper is organized as follows. The model description is given in Section 2. The numerical approach, its efficiency, and relevant computational problems are reviewed in Section 3. Simulation of a number of LED heterostructures and comparison with available experimental data is considered in Section 4. In Section 5, the results of the study are summarized and still open questions are discussed.

2. Model

An LED heterostructure is considered as a stack of uniform or graded-composition epitaxial layers coherently grown on an underlying template layer (normally, a buffer or an n-contact layer) in the direction z corresponding to the hexagonal axis (C-axis) of the wurtzite crystal. Thus, all the layers have the in-plane lattice constants equal to that of the template layer a_s. The thickness of the template layer is assumed to be much greater than the total thickness of the rest epilayers and, hence, the bending of the heterostructure as a whole can be neglected. The misfit strain components in a planar biaxially stressed layer are $\epsilon_1 = \epsilon_2 = -(a - a_s)/a$, $\epsilon_3 = -2\epsilon_1\ C_{13}/C_{33}$, where ϵ_i and C_{ij} are the components of strain and elastic stiffness tensor in the Voigt notation [12]. The unstrained lattice constant a of an $Al_xIn_yGa_{1-x-y}N$ alloy obeys the Vegard rule:

$$a = xa_{\mathrm{AlN}} + ya_{\mathrm{InN}} + (1 - x - y)a_{\mathrm{GaN}},$$

where a_{AlN}, a_{InN}, and a_{GaN} are the lattice constants of the binary constituents of the alloy.

There are two distinct effects of strain on the band diagram of an LED heterostructure. First, the tension (compression) decreases (increases) the energy bandgap. The bandgap variation may be significant: e.g., the difference in the bandgap of $In_{0.2}Ga_{0.8}N$ under the tensile and compressive strain equal in magnitude to 0.02 approaches $\sim$0.5 eV. The strain dependence of the bandgap is more steep under tension. While the energy of heavy holes depends weakly on the biaxial strain, a large strain-induced shift of light hole band is observed under tension [13]. Second, a strain generates a strong built-in electric field in the device structure because of piezoeffect. The only z-component of the piezoelectric polarization is essential to consider the LED heterostructure grown along the hexagonal axis of the crystal [14]

$$P^{\mathrm{pz}} = 2\epsilon_1\left(e_{13} - e_{33}\frac{C_{13}}{C_{33}}\right),$$

where e_{ij} are the components of the piezoelectric tensor in the Voigt notation.

Another source of the built-in electric field is the spontaneous polarization that may exist in polar semiconductors with wurtzite or lower crystal symmetry. The spontaneous polarization is directed along the C-axis of the crystal and is assumed to obey the Vegard law in III-nitride alloys

$$P^{\mathrm{sp}} = xP^{\mathrm{sp}}_{\mathrm{AlN}} + yP^{\mathrm{sp}}_{\mathrm{InN}} + (1 - x - y)P^{\mathrm{sp}}_{\mathrm{GaN}}.$$

The total polarization vector P^{tot} is the sum of these two contributions. In the case of InGaN layers coherently grown on GaN, the piezo-polarization is normally greater than the spontaneous one (except for low In-content alloys nearly lattice-matched with GaN). In contrast, the spontaneous polarization dominates in the AlGaN alloys grown on GaN. Generally, the sign of the piezo-polarization vector depends on the kind of strain (tensile or compressive) while that of the spontaneous polarization is controlled by the crystal polarity (III-faced, or N-faced).

2.1. Carriers concentrations

Electrons and holes obey generally the Fermi–Dirac statistics, i.e., their concentrations are defined by the expressions

$$n = N_{\mathrm{c}}\mathscr{F}_{1/2}\left(\frac{\varphi_n - E_{\mathrm{c}} + q\varphi}{kT}\right), \quad p = \sum_s N_{\mathrm{s}}\mathscr{F}_{1/2}\left(\frac{E_s - \varphi_p - q\varphi}{kT}\right), \tag{1}$$

where $\mathscr{F}_{1/2}$ is the Fermi integral

$$\mathscr{F}_{1/2}(\xi) = \frac{2}{\sqrt{\pi}}\int_0^\infty \frac{x^{1/2}}{1+\exp(x-\xi)}\,\mathrm{d}x,$$

φ_n, φ_p are the electron and hole quasi-Fermi levels, respectively, k is the Boltzmann constant, T is temperature, q is the electron charge, E_{c} is the conduction band edge. Summation in Eq. (1) is performed over three hole subbands ($s = \mathrm{hh}, \mathrm{lh}, \mathrm{so}$) corresponding to heavy holes (hh), light holes (lh), and split-off holes (so); thus E_{s} denotes the top edge of the respective valence subband. The effective densities of states of electrons in the conduction band, N_{c}, and holes in the respective valence subband, N_{s}, are given by the expressions

$$N_{\mathrm{c}} = 2m_n^{\perp}(m_n^{\parallel})^{1/2}\left(\frac{kT}{2\pi\hbar^2}\right)^{3/2}, \quad N_{\mathrm{s}} = 2m_s^{\perp}(m_s^{\parallel})^{1/2}\left(\frac{kT}{2\pi\hbar^2}\right)^{3/2},$$

where $\hbar$ is the Plank constant, $m_n^{\perp}$ and $m_n^{\parallel}$ are the in-plane and normal (along the z-axis) electron effective masses, $m_s^{\perp}$ and $m_s^{\parallel}$ are the in-plane and normal hole effective masses in the corresponding subband.

If the hole quasi-Fermi level lies above the valence band top $E_{\mathrm{v}} = \max_s(E_{\mathrm{s}})$, the hole concentration may be approximately calculated as

$$p = N_{\mathrm{v}}\mathscr{F}_{1/2}\left(\frac{E_{\mathrm{v}} - \varphi_p - q\varphi}{kT}\right), \quad N_{\mathrm{v}} = \sum_s N_{\mathrm{s}}\exp\left(-\frac{E_s - E_{\mathrm{v}}}{kT}\right).$$

In the opposite case, where the hole quasi-Fermi level lies well below the top of the lowest hole subband, the latter expression for the hole concentration remains valid, if the effective hole density of states, N_{v}, is taken equal to the sum $N_{\mathrm{hh}} + N_{\mathrm{lh}} + N_{\mathrm{so}}$.

2.2. Transport of electrons and holes

There are two alternative approaches to simulation of carrier transport in semiconductor devices [15]. One is a particle-based approach such as, e.g., the full-band ensemble Monte-Carlo method [16]. Its undeniable advantage is an accurate description of the carrier dynamics at an arbitrary ratio of the free carrier path to a characteristic device dimension. The price for the accuracy is the need in huge computational resources, somewhat alleviated by both advances in algorithms [17] and development of a low-cost hardware for parallel computations.

Another approach relies on continuum (macroscopic) models. Generally, the complexity of carrier transport descriptions reduces from rigorous kinetic models (the Boltzmann equation in the semiclassical case or its quantum-mechanical analog involving the Wigner function) through numerous quasi-hydrodynamical models to the DD ones [18,19]. The family of the continuum models is further extended by the development of hybrid models which couple models of various levels in different domains of the device [20]. Continuum models, when adequate, provide well over two orders of magnitude reduction of the CPU time compared to the particle-based approaches [21].

The DD model [22] could be derived formally from the Boltzmann equation (see for example [23]). Suggested over a half century ago in [24], it is based on the older ionic transport model by Nernst and Plank. Still, up to now it represents the most reasonable compromise between the computational efficiency and the accuracy of the description of underlying physical phenomena for a great variety of semiconductor devices [25].

In the case of a III-nitride LED, the DD model consist of the Poisson equation for the electrostatic potential φ, accounting for both spontaneous and piezopolarization, and the continuity equations for electrons and holes:

$$\nabla \cdot (\mathbf{P}^{\text{tot}} - \varepsilon_0 \hat{\varepsilon} \nabla \varphi) = q(N_{\text{D}}^{+} - N_{\text{A}}^{-} + p - n), \tag{2}$$

$$\nabla \cdot \mathbf{J}_n = -R, \quad \mathbf{J}_n = -\frac{\mu_n n}{q} \nabla \varphi_n, \tag{3}$$

$$\nabla \cdot \mathbf{J}_p = -R, \quad \mathbf{J}_p = \frac{\mu_p p}{q} \nabla \varphi_p. \tag{4}$$

Here ε_0 is dielectric permittivity of vacuum, $\hat{\varepsilon}$ is the static dielectric permittivity tensor, μ_n is the electron mobility, μ_p is the hole mobility assumed to be the same for all the valence subbands, N_{D}^{+} and N_{A}^{-} are the concentrations of ionized donors and acceptors:

$$N_{\text{D}}^{+} = \frac{N_{\text{D}}}{1 + g_{\text{D}} \exp\left(\frac{\varphi_n - E_{\text{c}} + q\varphi + E_{\text{D}}}{kT}\right)},$$

$$N_{\text{A}}^{-} = \frac{N_{\text{A}}}{1 + g_{\text{A}} \exp\left(\frac{E_{\text{v}} - q\varphi + E_{\text{A}} - \varphi_p}{kT}\right)},$$

where N_{D} and N_{A} are the total donor and acceptor concentrations, respectively, g_{D} and g_{A} are the degeneracy factors, E_{D} and E_{A} are the ionization energies of the impurities. The electron and hole fluxes, $\mathbf{J}_n$ and $\mathbf{J}_p$, are related to their partial electric current densities, $\mathbf{j}_n$ and $\mathbf{j}_p$, by the equations: $\mathbf{j}_n = -q\mathbf{J}_n$, $\mathbf{j}_p = q\mathbf{J}_p$.

The recombination rate R accounts for both non-radiative and radiative channels, i.e., $R = R^{\text{nr}} + R^{\text{rad}}$. The non-radiative carrier recombination is assumed to proceed primarily on the threading dislocation cores and can be accounted for within the Shokley–Read approach:

$$R^{\text{nr}} = \frac{np}{\tau_p(n + n_{\text{d}}) + \tau_n(p + p_{\text{d}})} \cdot \left[1 - \exp\left(-\frac{\varphi_n - \varphi_p}{kT}\right)\right],$$

where

$$n_{\text{d}} = n \cdot \exp\left(\frac{E_{\text{d}} - \varphi_n}{kT}\right), \quad p_{\text{d}} = p \cdot \exp\left(\frac{\varphi_p - E_{\text{d}}}{kT}\right),$$

and the electron (hole) lifetime, $\tau_{n(p)}$, is [10]

$$\tau_{n(p)} = \frac{1}{4\pi D_{n(p)} N_{\text{d}}} \left[\ln\left(\frac{1}{\pi a^2 N_{\text{d}}}\right) - \frac{3}{2} + \frac{2D_{n(p)}}{aV_{n(p)}S}\right].$$

Here, N_{d} is the dislocation density, $D_{n(p)} = (kT/q)\mu_{n(p)}$ is the diffusivity of electrons (holes), $V_{n(p)} = (3kT/m_{n(p)}^{\text{av}})^{1/2}$ is the carrier thermal velocity, $(m_{n(p)}^{\text{av}})^{3/2} = m_{n(p)}^{\perp}(m_{n(p)}^{\parallel})^{1/2}$, S is the fraction of electrically active sites in a dislocation core, and E_{d} is the energy level associated with the dislocation traps (see [10] for more detail).

The bimolecular radiative recombination rate is defined by the expression

$$R^{\text{rad}} = Bnp \cdot \left[1 - \exp\left(-\frac{\varphi_n - \varphi_p}{kT}\right)\right],$$

where B is the radiative recombination rate constant.

Let us associate the left edge of an LED heterostructure with the n-doped region and the right edge with the p-doped region. Then the boundary conditions for the Poisson equation (2) can be stated as follows:

$$\varphi_{\text{left}} = 0, \quad \varphi_{\text{right}} = \delta\varphi.$$

Here, $\delta\varphi$ is the sum of the applied bias and contact potential, the subscripts 'left' and 'right' refer to the position of the left and right edges of the LED heterostructure, respectively. The boundary conditions for the continuity equation (3) and (4) are derived from the electric neutrality condition, $N_{\text{D}}^{+} - N_{\text{A}}^{-} + p - n = 0$, assumed to be met at the edges of the LED heterostructure, i.e.,

$$\varphi_n = E_c + kT\mathscr{F}_{1/2}^{-1}\left(\frac{N_D^+ - N_A^- + p}{N_c}\right) - \varphi, \quad N_D > N_A,$$
$$\varphi_p = E_v - kT\mathscr{F}_{1/2}^{-1}\left(\frac{N_A^- - N_D^+ + n}{N_v}\right) - \varphi, \quad N_D < N_A$$

while the Neumann boundary conditions are set for the minority carrier quasi-Fermi levels.

An important mechanism that is presently ignored but should be incorporated into the transport model in the future is the tunneling current. A strong, up to ~3 MV/cm, polarization fields frequently create high but narrow local potential barriers near the structure interfaces, hindering the carrier injection into the active region (see Section 4 for more detail). In such cases, however, the contribution of the tunneling current may be comparable with that of the drift-diffusion current. There is, nevertheless, an evidence that the carrier tunneling enhanced by the dislocation-mediated deep-level states [26] is important at low/medium injection levels only, while under typical LED operation conditions the injection current produced by the drift-diffusion-recombination processes dominates [27,28]. Recent experiments [29] also show that the tunneling current may be suppressed in the high-quality structures even at the medium injection level due to the defect density reduction.

2.3. Light emission spectra

A band diagram and carrier concentrations obtained from the coupled solution of the Poisson and transport equations are then used to compute the light emission spectrum of an LED. In the present model, the spectral computations are decoupled from the band diagram analysis, i.e., the predicted conduction and valence band profiles are not used for making quantum-mechanical corrections of the radiative recombination rate. Only the principle channel, radiative recombination between the electron and hole states confined in the QW active region, is considered for simplicity. For this, the Schrödinger equations for electron and holes are solved with the potential energy profile determined from the self-consistent solution of the Poisson and DD transport equations (2)–(4). The complex valence band structure of the group-III nitride semiconductors is taken into account within the 8×8 Kane Hamiltonian [30]. The splitting of the heavy, light and split-off valence subbands in the centre of the Brillouin zone is assumed to be independent of the build-in electric field. Thus, the profiles of every valence subbands are equal to that predicted by the Poisson and DD equations.

The wave functions of electrons and holes are chosen in the form

$$u_n^{\sigma_n}\Psi_n(z)\exp(\mathbf{k}_n\cdot\mathbf{r}), \quad u_s^{\sigma_s}\Psi_s(z)\exp(\mathbf{k}_p\cdot\mathbf{r}), \quad s = \text{hh}, \text{lh}, \text{so},$$

where $u_n^{\sigma_n}$ and $u_s^{\sigma_s}$ are the spin-dependent Bloch amplitudes of electrons and holes corresponding to the center of the Brilluene zone, $\mathbf{k}_n$ and $\mathbf{k}_p$ are their in-plane quasi-moment vectors, Ψ_e and Ψ_s are the envelope functions. The Bloch amplitudes can be found as a superposition of the basis wave functions derived in [30]. The Schrödinger equation for the electron envelope function can be written in the approximate form

$$-\frac{\hbar^2}{2\langle m_n^{\parallel}\rangle}\frac{\mathrm{d}^2\Psi_n}{\mathrm{d}z^2} + (E_c - q\varphi)\Psi_n = E\Psi_n, \tag{5}$$

where $\langle m_n^{\parallel}\rangle$ is the longitudinal electron effective mass averaged over an individual QW with the weights proportional to the quasi-classical electron concentration (1), E is the energy of a confined electronic state. The averaging procedure accounts approximately possible variation of the electron effective mass across the heterostructure due to the composition variation of the material.

For heavy, light, and split-off holes similar equations are valid

$$\frac{\hbar^2}{2\langle m_s^{\parallel}\rangle}\frac{\mathrm{d}^2\Psi_s}{\mathrm{d}z^2} + (E_s + q\varphi)\Psi_s = E\Psi_s, \tag{6}$$

where $\langle m_s^{\parallel}\rangle$ is the longitudinal hole effective mass averaged over the individual QW.

Eqs. (5) and (6) are solved in the domain that includes the QW and the parts of surrounding barriers, large enough to set the homogeneous Dirichlet boundary conditions for Eqs. (5) and (6). The semiclassical wave-

function with the energy equal to the Fermi level in the QW is used to safely estimate the necessary size of the domain by the rate of the wavefunction decay in the barriers. The fourth-order finite difference (FD) scheme has been used for the solution of the eigenvalue problem for the Schrödinger equations.

Assuming vertical band-to-band transitions, the emission rate of photons with the frequency ω from an individual QW is given by the expression

$$w(\omega)=\frac{\pi}{\hbar}\left(\frac{q}{m_0c}\right)^2\sum_{\mathbf{k},s,\lambda}\sum_{\sigma_n,\sigma_s}\sum_{j,i}|\langle\Psi_n^{(j)}|\Psi_s^{(i)}\rangle|^2\cdot|\langle u_n^{\sigma_n}|\mathbf{A}_\lambda\cdot\hat{\mathbf{p}}|u_s^{\sigma_s}\rangle|^2\times f_{\mathbf{k}}^n f_{\mathbf{k}}^s\delta\left(\hbar\omega-E_g-E_n^{(j)}-E_s^{(i)}-\frac{\hbar^2k_\perp^2}{2\mu_s^\perp}\right), \tag{7}$$

where indexes j and i mark the confined states of electrons and holes in the QW, m_0 is the electron mass in vacuum, c is the light velocity in vacuum, $\mathbf{A}_\lambda$ is the vector potential of the electromagnetic wave with polarization denoted by the subscript λ, $\hat{\mathbf{p}}$ is the momentum operator, $f_{\mathbf{k}}^n$ and $f_{\mathbf{k}}^s$ are the distribution functions of electrons and holes corresponding to the quasi-momentum vector $\mathbf{k}=\mathbf{k}_n=k_{\mathbf{p}}$, E_g is the bandgap of the semiconductor, $E_n^{(j)}$ and $E_s^{(i)}$ are the energies of confined electron and hole states, and $\mu_s^\perp=m_n^\perp m_{p,s}^\perp/(m_n^\perp+m_{p,s}^\perp)$ is the in-plane reduced effective mass of the carriers; $\delta(x)$ is the delta-function. In Eq. (7), summation is performed over all the $\mathbf{k}$-states, valence subbands, two orthogonal light polarizations, spin states of electron and holes, σ_n and σ_s, and electron/hole states confined in the QW.

To account for a uniform spectrum broadening, the photon emission rate is convoluted with a Lorentzian $(\Gamma/\pi)[(E-E')^2+\Gamma^2]^{-1}$, where Γ is the broadening parameter.

3. Numerical implementation

The drift-diffusion equations (2)–(4), being a singular perturbed problem, can exhibit both boundary and interior layers with a rapid variation of the carrier concentrations and/or electric field [31,32]. Moreover, the stiffness of the DD equations increases nonlinearly with the bandgap of the material. Additional difficulty typical of nitride devices is a strong build-in electric field due to both spontaneous and piezo-polarization, resulting in a huge transformation of the device band diagram. Although the DD model was widely used for decades (see for example [33]), a rigorous analysis of the underlying equation system has been carried out under quite restrictive assumptions only (decoupled problems for the electric potential and carrier concentrations, no generation-recombination processes, Boltzmann statistics, etc.) and mostly deals with the existence rather than with the uniqueness of the solution [34–37]. Moreover, it was found that the solutions of one-dimensional "voltage driven" problem are not unique in some particular cases [38]. Thus, the choice of an appropriate numerical model implementation is critical for getting reliable results.

3.1. Approximation of the DD equations

The DD model can be formulated using quite different sets of mutually dependent variables [39]

- "natural" concentration-potential variables: $[\varphi,n,p]$,
- quasi-Fermi level formulation: $[\varphi,\varphi_n,\varphi_p]$,
- Slotboom formulation [40]: $[\varphi,u,v$; where $u=n\cdot\exp(-q\varphi/kT)$ and $v=p\cdot\exp(q\ \varphi/kT)]$.

The latter choice is attractive mathematically since the carrier continuity equations are self-adjoint and linear in u and v [32], which simplifies the analysis of the DD model in the case of the Boltzmann statistics. Another advantage of the Slotboom variables is the symmetry and positive definiteness of the matrix of the linearized discrete equations. However, the coefficients of these equations depend exponentially on φ, φ_n, φ_p. That is why the Slotboom variables are mainly used for analytical studies. An extension of the formulation to the case of a heavy doping of a semiconductor (Fermi–Dirac statistics) is cumbersome and unnatural.

It is well known that the polynomial finite-difference (FD) schemes do not provide a uniform convergence with respect to a small parameter [31]. To overcome this problem, the exponentially fitted FD

schemes have been suggested in [41–43]. The idea is to exploit the exact (fundamental) solution of the homogeneous equation for discretization of the continuity equations written in terms of the "natural" variables. Our attempt to use the Scharfetter–Gummel scheme [43] for analysis of the carrier transport in nitride LED structures was only successful for low doping levels and moderate biases. If the doping and the voltage increase, spurious current oscillations near abrupt structure interfaces start to occur. At least partly, this artifact is the result of the finite length of a computer representation of the floating point numbers, since the oscillation magnitude diminishes with the increase of the word length from 8 to 12 bytes. However, even the latter accuracy proved to be insufficient for highly doped wide-bandgap heterostructures at all biases of interest.

The quasi-Fermi level formulation is the most natural one for the degenerate case and, as well as Slotboom one, "regularize" the problem by reducing the dynamic range of the unknown variation. In the ordinary finite-element (FE)/finite-difference methods an asymptotic order of the derivative approximation is less by unity then that of the variable itself since the differentiation procedure lowers accuracy. On the other hand, one is often no less interested in the detailed distribution of the electric field and partial current densities across the heterostructure. Thus, the mixed FE method (FEM) [32] is employed in our study. The one-dimensional DD equations are re-written as a system of the first-order equations in the electrostatic potential φ, z-component of the electrostatic induction vector D_z, the electron and hole quasi-Fermi levels φ_n, φ_p, and the corresponding carrier fluxes along the z-coordinate J_{nz}, J_{pz} (the subscript "z" is omitted in the following equations):

$$\begin{aligned} D'_z &= q\left[N_D^+(\varphi,\varphi_n) - N_A^-(\varphi,\varphi_p) + p(\varphi,\varphi_p) - n(\varphi,\varphi_n)\right], \\ \varphi'_z &= (P^{\text{tot}} - D)/\varepsilon_0\varepsilon_{33}, \end{aligned} \tag{8}$$

$$\begin{aligned} (J_n)'_z &= -R(\varphi,\varphi_n,\varphi_p), \\ J_n &= -\frac{\mu_n n(\varphi,\varphi_n)}{q}(\varphi_n)'_z, \end{aligned} \tag{9}$$

$$\begin{aligned} (J_p)'_z &= -R(\varphi,\varphi_n,\varphi_p), \\ J_p &= \frac{\mu_p p(\varphi,\varphi_p)}{q}(\varphi_p)'_z. \end{aligned} \tag{10}$$

In Eqs. (8)–(10), G'_z denotes the derivative of the variable G by z. These pairs of equations, expressing the conservation of charge, electron and holes, respectively, have the same structure as the equations

$$\begin{aligned} (G)'_z &= Q(z), \\ G &= A(z)f'_z + B(z), \end{aligned} \tag{11}$$

where the first one is the *balance* equation, while the second one is the linear combination of the *kinematic* and the *constitutive* equations (for example, for the charge conservation subsystem the latter two equations are $-\nabla\varphi = \mathbf{E}$ and $\mathbf{D} = \varepsilon_0\varepsilon_{33}\mathbf{E} + \mathbf{P}^{\text{tot}}$). A derivation of discrete FE equations proceeds in the standard way (see for example [44]): the differential equations are transformed into a weak form via multiplying them by test functions and integrating the product over the computational domain. The basis functions of the mixed FEM for the generic system (11) should belong to proper spaces (to the space L^2 of the square integrable functions for f and to the space $\mathbf{H}$(div) of the functions with the square integrable derivatives for G) [32]. Thus, $f(\varphi,\varphi_n,\varphi_p)$ can be approximated by a set of the piecewise constant functions

$$f(z) = \sum_i f_i M_i(z)$$

while $G(D, J_n, J_p)$ – by a set of the piecewise linear functions

$$G(z) = \sum_i f_i N_i(z).$$

Defining $\Omega = (z_i, z_{i+1})$, $\bar{\Omega} = [z_i, z_{i+1}]$, the basis functions $M_i(z)$ and $N_i(z)$ can be evidently written as

$$M_i(z) = \begin{cases} 1 & \text{if } z \in \Omega_i, \\ 0 & \text{if } z \notin \Omega_i, \end{cases} \quad N_i(z) = \begin{cases} \frac{z - z_{i-1}}{z_i - z_{i-1}} & \text{if } z \in \bar{\Omega}_{i-1}, \\ \frac{z_{i+1} - z}{z_{i+1} - z_i} & \text{if } z \in \bar{\Omega}_i, \\ 0 & \text{if } z \notin \bar{\Omega}_{i-1} \cup \bar{\Omega}_i. \end{cases}$$

The use of the zero-order elements for the primary variables and of the first-order elements for the fluxes may be counter-intuitive, but it is just this unique feature of the mixed FEM that permits a more accurate description of the electric field and current densities, which is often of a primary interest.

3.2. Solution of the discrete DD equations

There are two basic approaches to the solution of coupled nonlinear equations like the discretized DD ones

$$\mathbf{F}(\mathbf{\Phi}) = 0, \tag{12}$$

where

$$\mathbf{F} = (F_\varphi, F_{\varphi_n}, F_{\varphi_p})^{\mathrm{T}}, \quad \mathbf{\Phi} = (\Phi_\varphi, \Phi_n, \Phi_p)^{\mathrm{T}}$$

for the ordinary FD/FE methods and

$$\mathbf{F} = (F_\varphi, F_D, F_{\varphi_n}, F_{J_n}, F_{\varphi_p}, F_{J_p})^{\mathrm{T}}, \quad \mathbf{\Phi} = (\Phi_\varphi, \Phi_D, \Phi_n, \Phi_{J_n}, \Phi_p, \Phi_{J_p})^{\mathrm{T}}$$

for the FEM approach; superscript "T" denotes a transposition.

The first approach is a simultaneous solution of the equations. The advantage of the well-known Newton method (i is the iteration number)

$$\mathbf{\Phi}^{i+1} = \mathbf{\Phi}^i - \mathbf{J}^{-1}(\mathbf{\Phi}^i)F(\mathbf{\Phi}^i), \quad \mathbf{J} = \frac{\partial \mathbf{F}}{\partial \mathbf{\Phi}}$$

over other techniques is its quadratic convergence property. Unfortunately, this method has two drawbacks. One, a high cost of the Jacobian **J** computation and the necessity to solve a large linear system, can be partly overcome by a "lazy" updating of **J** or/and its approximation [45]. Another drawback is more severe: the Newton method is extremely sensitive to an initial guess. General methods such as the variable metric one, being tolerant to the initial guess, are applicable in practice to the systems with reduced number of equations [46].

The second approach is a segregated solution of the underlying equations. In this method known as Gummel's method ("Gummel's map") [47] the three discrete equation systems (Poisson, electron, and hole continuity equations) derived within the ordinary FD/FE methods are solved sequentially in a Gauss–Seidel fashion:

$$\varphi(\Phi_\varphi^{i+1}, \Phi_n^i, \Phi_p^i) = 0, \tag{13}$$

$$F_{\varphi_n}(\Phi_\varphi^{i+1}, \Phi_n^{i+1}, \Phi_p^i) = 0, \tag{14}$$

$$F_{\varphi_p}(\Phi_\varphi^{i+1}, \Phi_n^{i+1}, \Phi_p^{i+1}) = 0. \tag{15}$$

Fixed points of such a mapping correspond to the solutions to the DD equations [36]. The attractive property of the Gummel method is a robustness with respect to an initial approximation. There is an evidence, however, that the approach could be inadequate near the breakdown voltage when the electron and hole continuity equations are strongly coupled due to large generation-recombination terms [48]. It should be noted that the solution of individual equations in the Gummel's map can still be performed using Newton method, while the method itself could be combined with Newton method as an aid to get a good initial guess for the latter [49]. In the case of the FEM the segregated solution procedure equations (13)–(15) transform into the following one:

$$\begin{aligned} F_\varphi(\Phi_\varphi^{i+1}, \Phi_D^{i+1}, \Phi_n^i, \Phi_{J_n}^i, \Phi_p^i, \Phi_{J_p}^i) = 0, \\ F_D(\Phi_\varphi^{i+1}, \Phi_D^{i+1}, \Phi_n^i, \Phi_{J_n}^i, \Phi_p^i, \Phi_{J_p}^i) = 0, \end{aligned} \tag{16}$$

$$\begin{aligned} &F_{\varphi_n}(\Phi_\varphi^{i+1},\Phi_D^{i+1},\Phi_n^{i+1},\Phi_{J_n}^{i+1},\Phi_p^i,\Phi_{J_p}^i)=0,\\ &F_{J_n}(\Phi_\varphi^{i+1},\Phi_D^{i+1},\Phi_n^{i+1},\Phi_{J_n}^{i+1},\Phi_p^i,\Phi_{J_p}^i)=0,\end{aligned} \tag{17}$$

$$\begin{aligned} &F_{\varphi_p}(\Phi_\varphi^{i+1},\Phi_D^{i+1},\Phi_n^{i+1},\Phi_{J_n}^{i+1},\Phi_p^{i+1},\Phi_{J_p}^{i+1})=0,\\ &F_{J_p}(\Phi_\varphi^{i+1},\Phi_D^{i+1},\Phi_n^{i+1},\Phi_{J_n}^{i+1},\Phi_p^{i+1},\Phi_{J_p}^{i+1})=0,\end{aligned} \tag{18}$$

Thus, three nonlinear subsystem equations (16)–(18) for $(\varphi, D), (\varphi_n, J_n)$, and (φ_p, J_p) are to be solved sequentially until the prescribed convergence condition is met. In the present paper, the approach based on the homotopy method is adopted, following [50]. The idea of this method called also the *continuation* method or *path following* [51] is to consider the following underdetermined equation system:

$$\mathbf{H}(\mathbf{\Phi}, \lambda) = 0$$

instead of Eq. (12). Here, $\mathbf{H} : \mathbb{R}^K \otimes \mathbb{R} \to \mathbb{R}^K$ is a smooth map that implicitly defines a curve as a function of parameter λ. The most common use of this method is to define

$$\mathbf{H}(\mathbf{\Phi}, \lambda) = \mathbf{F}(\mathbf{\Phi}) - \lambda\mathbf{F}(\mathbf{\Phi}_1)$$

and follow the path from $(\mathbf{\Phi}_1, 1)$ to the solution of the initial problem $(\mathbf{\Phi}, 0)$. In [50] the homotopy method is implemented as an artificial transient problem

$$\mathbf{H}(\mathbf{\Phi}, \lambda) = \mathbf{F}(\mathbf{\Phi}) + \frac{\mathbf{\Phi}}{\lambda}$$

so the solution is determined as the limit at $\lambda \to \infty$. Thus, the equations can be re-written in accordance with the following modification (illustrated below for the generic subsystem)

$$\begin{aligned} &\frac{f^{k+1} - f^k}{\tau^k(z)} + (G)'_z = Q(z),\\ &G = A(z)f'_z + B(z).\end{aligned} \tag{19}$$

The choice of the local fictious time steps $\tau^k_\varphi(z)$, $\tau^k_{\varphi_n}(z)$, and $\tau^k_{\varphi_p}(z)$ for the discretized equations is discussed in detail in [50].

3.3. Verification

The above model of carrier transport and light emission has been implemented into the SiLENSe code (simulator for light emitters based on nitride semiconductors) [52]. In this section, we discuss the necessary stages of a numerical tool development – verification (an assessment of the correctness of the model implementation) and validation (an assessment of the adequacy of the model to the reality) [53].

Verification is primarily a mathematical issue. The major sources of the errors have been listed in [54]: insufficient spatial and/or temporal discretization convergence, insufficient convergence of an iterative procedure, computer round-off, and programming errors. The errors of the last type are the most difficult to detect and fix when the code executes without an obvious crash yielding "*moderately incorrect results*" [54]. The study reported in [55] revealed a surprisingly large number of such faults in the tested both commercial and research scientific codes regularly used by their users. Standard verification approaches are generally based on either comparison of a numerical and an exact solutions or/and computations followed by the grid refinement.

Grid convergence for a simple structure (GaN p–n junction with the donor and acceptor concentrations of 10^{18} cm^{-3}) is illustrated by Fig. 1. Different norms could be used to measure the solution error [56]. Normally, the error e_f of the variable f is estimated in the Euclidian norm (2-norm) L^2

$$e_f^{L^2} = \left[\frac{1}{N}\sum_{i=1}^{N}(f_i - f_{\text{bench}}(z_i))^2\right]^{1/2},$$

where f_i is the computed value at the point z_i and $f_{\text{bench}}(z_i)$ is the "benchmark" solution at this point, N is the number of points. This measure, however, could be misleading in simulation of the semiconductor devices

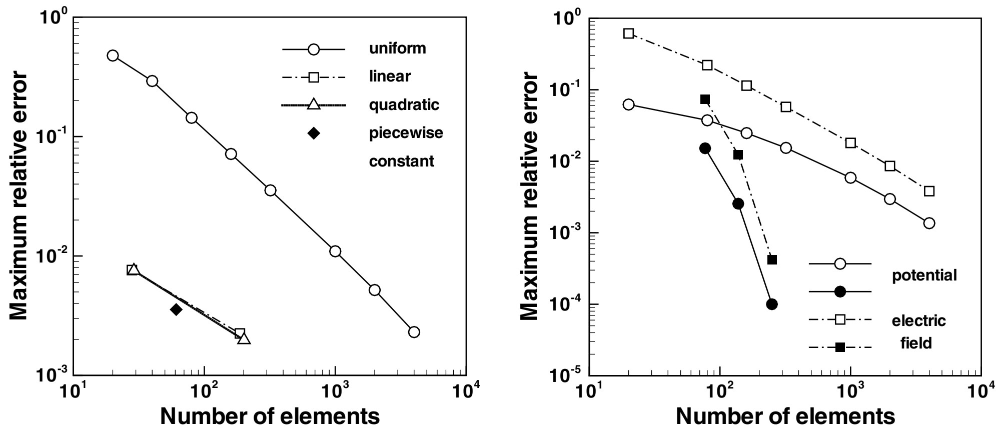

Fig. 1. Convergence tests for GaN p–n junction (left) and GaInN/GaN heterojunction (right).

when thicknesses of individual layers are comparable with the space-charge region widths. Indeed, the electric field and the carrier concentration distributions exhibit in complex heterostructures numerous sharp maxima and minima. Thus, it is anticipated that it is more useful for the device engineer to know how well the numerical method reproduces these singularities, i.e., the maximum norm (∞-norm) L^{∞}

$$e_f^{L^\infty} = \max_i |(f_i - f_{\text{bench}}(z_i))|$$

seems to be more appropriate. This norm for the electric field scaled by the variable value in the position of maximum error, i.e., the "∞-norm" of the *relative* error

$$\delta_E = \frac{e_E^{L^\infty}}{E_{i^*}}, \quad i^* : e_E^{L^\infty} = E_{i^*} - E_{\text{bench}}(z_{i^*})$$

is shown in Fig. 1 for a uniform and different non-uniform grids versus the number of elements N. The "benchmark" solution is obtained on the uniform grid containing 20,000 elements. This plot underlines one of the advantages of the mixed element formulation – tolerance to relative sizes of neighboring elements: the results marked by "diamond" are obtained on the grid with the piecewise constant element size and the aspect ratio of the neighboring elements $\Delta z_i/\Delta z_{i+1}$ up to 50.

Another test case refers to the GaInN/GaN heterojunction including n-GaN doped with 10^{19} cm^{-3} donors and p-GaInN doped with 10^{18} cm^{-3} acceptors. Under forward bias, this structure provides local extremuma in the electric potential, electric field, and carrier concentrations. The maximum relative error for the first two variables as a function of the number of elements is also displayed in Fig. 1. Here, the open symbols correspond to a uniform grid, the filled ones – to grids with variable steps (the maximum aspect ratio $\max\{\Delta z_i\}/\min\{\Delta z_i\} = 2500$, the aspect ratio for the neighboring elements $\Delta z_i/\Delta z_{i+1} = 10$). One more advantage of the FEM scheme, an accurate reproduction of derivatives (in particular, of electric field that is the derivative of the electric potential), is evident from Fig. 1.

For a number of reasons, direct validation of the 1D numerical model of the LED heterostructure is not easy. First, in practice a strong lateral non-uniformity of the current density and light emission intensity is observed because of the planar design of an LED chip (see for example [3,57]). Actually, the current density may vary by the order of magnitude in the p–n junction plane. Second, InGaN QWs exhibit remarkable composition fluctuations on a microscopic scale, forming In-rich regions of tens nanometer in lateral dimension and a few nanometer in height. This results in considerable local variation of the light intensity due to the interplay of radiative and non-radiative recombination. For instance, the fluctuations of internal quantum efficiency from 10% to 50% have been reported in [58]. Third, the published descriptions of the LED heterostructures are rarely complete, first of all, with respect to the QW composition and active layer doping. The latter issue is extremely important if co-doping is employed. In particular, simultaneous doping of the active layer with Si and Zn result in a large, ~0.4–0.5 eV, shift of the emission peak [59] and evidently

affects the internal quantum efficiency of the LED structure as a whole. All these details of the LED design are frequently obscure, which leads to an uncertainty when comparing the theoretical and experimental results.

Hence, the questions are: how mature is the developed numerical approach? could it provide new knowledge and serve as an aid in the development and/or optimization of a III-nitride LED structure? An attempt to answer these questions using the available data on LED heterostructures and their operational conditions is reported in the next section of the paper.

4. Examples of simulations

Accurate determination of materials properties is the factor largely affecting the predictability of simulations. Unfortunately, the materials properties of group-III nitrides are known not so well as those of conventional III–V compounds and silicon. Up to now, the bandgaps of InN and InGaN ternary compounds are the subject of extensive discussion in literature (see e.g. [60]). The values of spontaneous electric polarization of binary nitrides are obtained by first-principle computations only (see [61] and references therein). There is even considerable scatter between various theoretical estimates for carrier mobilities obtained by the Monte-Carlo method (see for example [62,63], published in the same journal issue). The measured carrier mobilities, however, depend strongly on the growth conditions and, therefore, should be rather borrowed from experiment.

Accounting for the importance of this issue for the validation of the III-nitride LED model, we summarize below the material properties of group-III nitrides used in our simulation of carrier transport and light emission.

4.1. Material properties

In this paper, all the material characteristics of nitride alloys are approximated by the Vegard rule

$$f_{\mathrm{Al}_x\mathrm{Ga}_y\mathrm{In}_{1-x-y}\mathrm{N}} = xf_{\mathrm{AlN}} + yf_{\mathrm{GaN}} + (1-x-y)f_{\mathrm{InN}},$$

the only exception being the bandgap of the materials for which a quadratic approximation is used:

$$(E_g)_{\mathrm{Al_xGa_yIn_{1-x-y}N}} = x(E_g)_{\mathrm{AlN}} + y(E_g)_{\mathrm{GaN}} + (1-x-y)(E_g)_{\mathrm{InN}} - xyb_{\mathrm{Al-Ga}} - x(1-x-y)b_{\mathrm{Al-In}} - y(1-x-y)b_{\mathrm{Ga-In}}, \quad (20)$$

where the bowing parameters $b_{\mathrm{Al-Ga}}$, $b_{\mathrm{Al-In}}$, $b_{\mathrm{Al-In}}$, based on the analysis of [2,64–68], are taken equal to 1.0, 4.5, and 1.2 eV for AlGaN, AlInN, and GaInN, respectively. The materials characteristics of binary nitrides used in our computations are given in Table 1. These values have been chosen after the analysis of the published data: [2,69,70] on the lattice constant, [2,69,71,72] on the elastic constants, and [73,74] on the dielectric permitivity. The bandgaps are taken from [75], while the parameters related to the piezo-polarization – from [76]. Effective electron and hole masses in the binary nitrides at 300 K (Table 2) are borrowed from [77] for AlN, InN and from [30] for GaN. The data on the bandgap offsets in III-nitride heterostructures are reviewed in [2]. On the basis of the data, one can derive that the valence band offset in all nitride compounds is equal to

Table 1
Properties of binary nitrides

Parameter	Symbol	Units	AlN	GaN	InN
Lattice constant	a	nm	0.3112	0.3188	0.3540
Static dielectric constant	ϵ_{33}		8.5	8.9	15.3
Spontaneous polarization	P^{sp}	C/m^2	−0.081	−0.029	−0.032
Piezoelectric constant	e_{13}	C/m^2	−0.58	−0.33	−0.22
Piezoelectric constant	e_{33}	C/m^2	1.55	0.65	0.43
Elastic constant	C_{13}	GPa	115	105	95
Elastic constant	C_{33}	GPa	385	395	200
Bandgap	E_{g}	eV	6.2	3.4	0.7

Table 2
Effective masses of electrons and holes in binary nitrides

	AlN		GaN		InN	
	‖	⊥	‖	⊥	‖	⊥
m_n	0.25	0.25	0.2	0.2	0.1	0.1
$m_{p,hh}$	1.95	0.25	1.1	0.15	1.35	0.1
$m_{p,hl}$	1.95	2.58	1.1	1.65	1.35	1.45
$m_{p,so}$	0.23	1.93	0.15	1.1	0.09	1.54

~30% of the full bandgap offsets. This value, which agrees well with the theoretical predictions of [78], is taken in our simulations.

For simplicity, we used the same donor and acceptor ionization energies, $E_D = 13$ meV and $E_A = 170$ meV, and the radiative recombination rate constant $B = 2.4 \times 10^{-11}$ cm^3/s [79] for all the nitride alloys. The acceptor and donor g-factors, $g_D = 2$ and $g_A = 4$, and the spectrum broadening parameter $\Gamma = 20$ meV have been taken in all computations.

4.2. Blue single-quantum-well LED structures

4.2.1. Structure with compositionally uniform layers

This heterostructure has been described in [27] (its parameters are given in Table 3). The impurity concentrations are chosen on the basis of previous publications by Nakamura. The structure is assumed to be grown on a Ga-faced surface (Ga-polarity), the operation temperature is taken to be of 300 K, the chosen threading dislocation density $N_d = 10^8$ cm^{-2} is by the order of magnitude lower than the typical dislocation density in the LED heterostructures grown by metalorganic chemical vapor deposition (MOCVD). The reduced N_d used in the simulations accounts, at least qualitatively, for the effect of In composition fluctuations responsible for the carrier capture in the In-rich regions avoiding their non-radiative recombination on threading dislocations cores [80].

The results of simulations of the SQW LED heterostructure for the typical current density of $j = 30$ A/cm^2 are shown in Figs. 2–6. A specific feature clearly seen in the band diagram (Fig. 2(a)) is the drop of the electron quasi-Fermi level φ_n near the InGaN QW. Actually, φ_n varies continuously but very steeply in the n-GaN contact layer near the InGaN/GaN (left) interface. This effect, described earlier in [81] with reference to an AlGaAs/GaAs laser heterostructure, originates from a drastic lowering of the electron concentration caused by the local potential barrier appeared at the InGaN/GaN interface due to its negative polarization charge. The higher the current density through the diode, the higher is the drop of the electron quasi-Fermi level, until a high injection level is reached at an increased forward bias, enhancing screening of the built-in electric field.

In contrast to conventional III–V compounds, the above effect is much more pronounced in III-nitride materials because of a huge polarization charge accumulated on the left InGaN/GaN interface (the charge corresponds to the sheet concentration of ~10^{13}–10^{14} cm^{-2} depending on the InGaN composition). In particular, for green LEDs the DD model predicts even formation of a nearly insulating layer at this interface, which does not allow flowing of a remarkable current through the device. In practice, however, a tunneling current starts to dominate under these conditions, which is not allowed in the current model.

Table 3
Blue InGaN SQW LED structure

Layer	Thickness (nm)	Material	Type	Doping (cm^{-3})
n-Contact	600	GaN	n	3×10^{18}
QW	3.5	$In_{0.2}Ga_{0.8}N$	UID	–
p-Emitter	100	$Al_{0.1}Ga_{0.9}N$	p	7×10^{19}
p-Contact	600	GaN	p	7×10^{19}

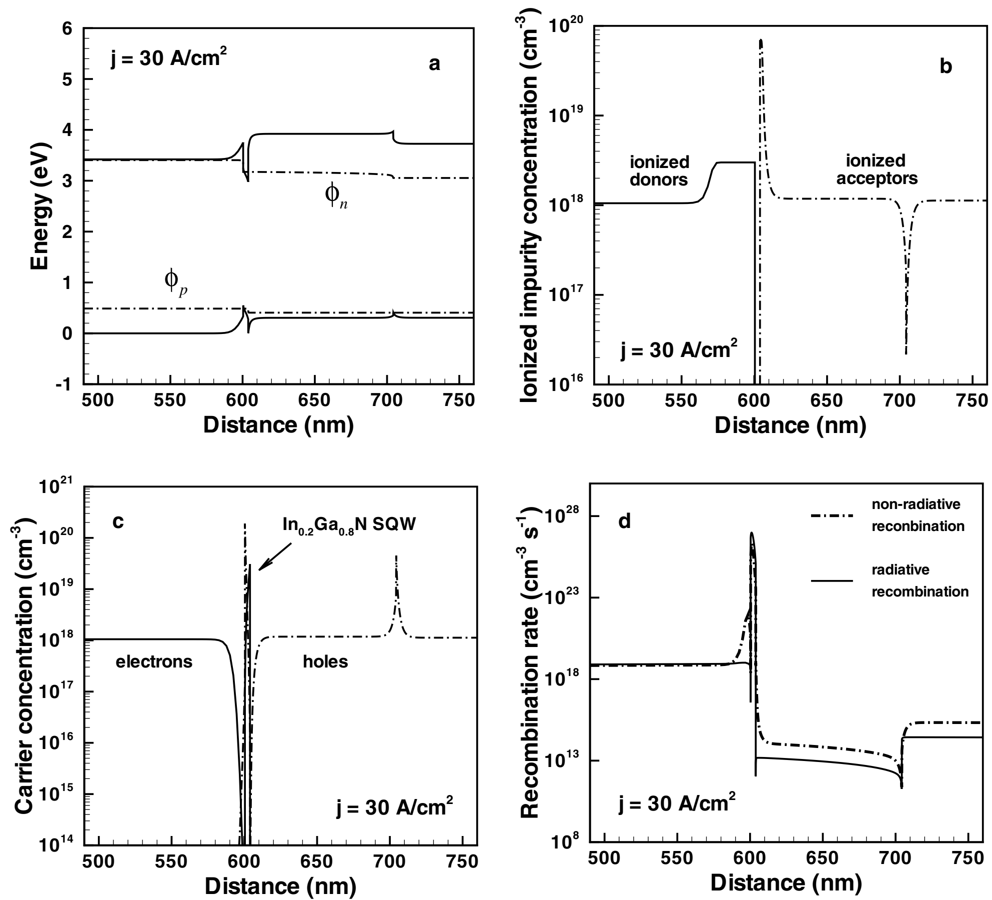

Fig. 2. InGaN SQW LED structure at $j = 30$ A/cm^2: (a) band diagram (φ_n and φ_p denote the quasi-Fermi levels of electrons and holes), (b) ionized impurity concentrations, (c) carrier concentrations, and (d) recombination rates.

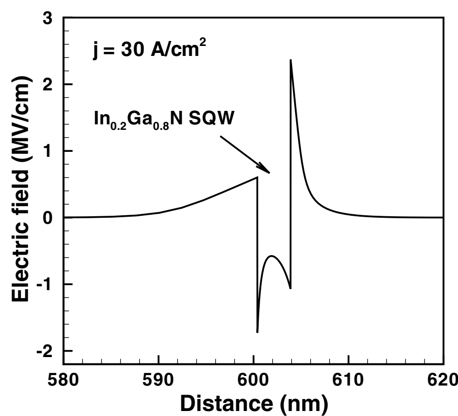

Fig. 3. InGaN SQW LED structure: electric field distribution.

The ionized donor and acceptor concentrations (Fig. 2(b)) change weakly with the forward bias. However, due to a high Mg acceptor ionization energy, the ionization efficiency of acceptors may vary up to two orders of magnitude depending on the local hole quasi-Fermi level position.

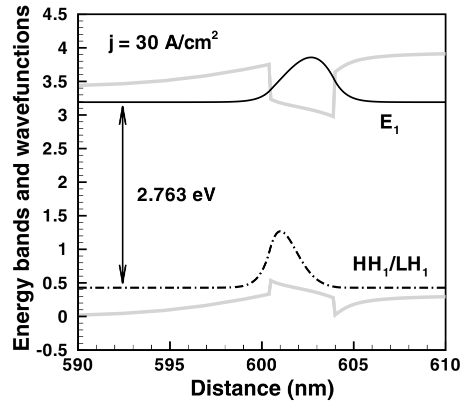

Fig. 4. InGaN SQW LED structure: ground-state electron and hole wave functions.

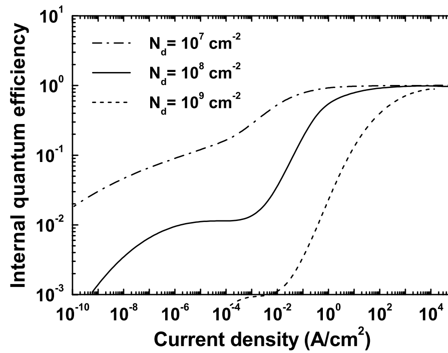

Fig. 5. IQE of InGaN SQW LED structure as a function of current density computed for various dislocation densities.

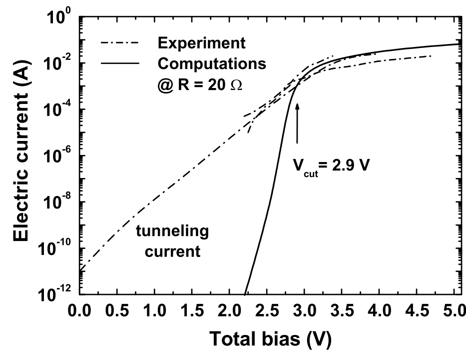

Fig. 6. InGaN SQW LED: comparison of calculated and measured current-voltage characteristics.

The distribution of carrier concentrations and recombination rates are shown in Figs. 2(c) and (d). Because of the barrier at the left InGaN/GaN interface, electrons penetrate to the InGaN SQW much poorer than holes. Therefore, the efficiency of the carrier injection into the InGaN active layer is limited by electrons rather than by holes as it might be expected from a lower hole concentration in the p-AlGaN emitter. Both electrons and holes are seen to be poorly confined near the InGaN SQW (Fig. 2(a)) because of low barriers created in the p-AlGaN and n-GaN claddings, respectively.

Due to a high dislocation density in the LED structure, the non-radiative recombination of the non-equilibrium carriers prevails the radiative one at a lower injection level. As the injection level increases, the carrier recombination becomes localized in the InGaN quantum well and the radiative recombination starts to dominate (Fig. 2(d)). The tail of the non-radiative recombination in the n-GaN contact layer is caused by the hole penetration to this region, which increases with bias.

The electric field in the LED structure is predicted to be as high as ~2–3 MV/cm (Fig. 3). The field is found to decrease considerably with bias both in the quantum well (due to screening by the non-equilibrium carriers) and in the emitters (due to narrowing of the space-charge region). Actually, the electric field in the QW is a superposition of the positive built-in p–n junction field and the negative polarization field. Therefore, the conventional estimates of the field based on the polarization charges and QW thickness only normally fail even at a low bias.

The electron and hole wave functions corresponding to their ground states in the InGaN SQW are plotted in Fig. 4. It is seen that electrons and holes are shifted to the opposite edges of the QW due to the Stark effect. Because of the reduced overlap of the electron and hole wave functions, the radiative recombination rate is expected to be lower than in the respective InGaN bulk material. However, in addition to the ground electronic states, up to 6–8 excited states are found to exist for holes and, at a high bias, an additional excited state appears also for electrons. Under these conditions, the reduction in the radiative recombination rate becomes not so evident and the Stark effect may be, at least partly, accounted for via separation of the electron and hole concentration peaks (see Fig. 2(c)). In our opinion, this issue requires more detailed examination.

The IQE of an LED structure is defined as the the ratio of the radiative recombination rate integrated over the structure to the carrier (electron or hole) flux in the respective contact layer. The IQE depends strongly on the dislocation density N_d due to competition of the radiative and non-radiative carrier recombination (Fig. 5). Though the typical value of N_d in the MOVPE-grown heterostructures is about 10^9 cm^{-2}, the effective dislocation density controlling the non-radiative recombination is lower due to the In-composition fluctuations. Therefore for InGaN LEDs, the dislocation density N_d is rather an adjustable parameter that requires careful estimation from observations. For SQW LED considered, the value $N_d = 10^8$ cm^{-2} provides the saturation of the light emission efficiency at $j \sim 10$ A/cm^2, in accordance with the maximum of the LED external efficiency measured in [27]. Therefore, just this value is chosen for further simulations. In this case, the corresponding non-radiative life times due to carrier recombination on threading dislocations in the active region are: $\tau_n = 9$ ns and $\tau_p = 46$ ns.

Generally, the non-radiative carrier recombination on point defects should be also included in the recombination model, in addition to the dislocation-mediated recombination. The estimates of the respective electron and hole life times made from the carrier diffusion lenghts measured in low-dislocation GaN (see references cited in [10]) show that they are in the range of ~10–100 ns, if the dislocation density is less than ~10^7–10^8 cm^{-2}. In our study, we neglect this mechanism of the non-radiative recombination in order to clarify better the impact of dislocations on the LED efficiency.

At the current densities $j > 10$ A/cm^2, fall down of the external efficiency rather than its saturation is observed in experiment [27]. The efficiency reduction with current cannot be explained within the existing model and requires further efforts to understand. In particular, self-heating of the LED structure may be responsible for the efficiency reduction at high currents (see [82] where a comparison of dc and pulsed LED operation has been reported, supporting the latter idea).

Simulated dependence of the current density j upon p–n junction bias U_b allows calculation of the I–V characteristic of the LED by using the relationships

$$I = jA, \quad U_{\text{tot}} = U_b(j) + j \cdot (AR_s + \rho_n + \rho_p),$$

where I is the total current, U_{tot} is the total bias applied to the diode, A is the contact area, ρ_n and ρ_p are the specific n- and p-contact resistances, respectively, and R_s is the series resistance of the LED largely controlled by the lateral current spreading in the chip. Comparison of the I–V characteristic of the SQW LED measured on various samples [27,83] with those calculated for the contact area $A = 10^{-3}$ mm^2 and the serial resistance $R_s = 20\ \Omega$ is presented in Fig. 6. It can be seen that the implemented model satisfactory describes the injection-limited current ($U_{\text{tot}} > 2.8$ V). At the biases less than 2.8 V, tunneling current is found experimentally to dominate in the LED structure, which is not allowed for in the DD model.

Table 4
Graded-composition blue SQW LED structure

Layer	Thickness (nm)	Material	Type	Doping (cm^{-3})
n-Contact	700	GaN	n	3×10^{18}
n-Emitter	30	Graded InGaN	n	3×10^{18}
QW	3.5	$In_{0.2}Ga_{0.8}N$	UID	–
p-Emitter	50	Graded AlGaN	p	5×10^{19}
p-Contact	500	GaN	p	5×10^{19}

Detailed analysis of the effect of the crystal polarity on the LED performance has been reported in [84]. It has been found that in contrast to the Ga-faced LED (Fig. 2), The N-faced heterostructure is free from the barriers hindering the carrier injection in the active region due to the inversion of signs of the polarization charges at the SQW interfaces. The improved injection efficiency and electron confinement result in a lower turn-on voltage compared to the Ga-faced structure. On the other hand, in the N-faced LED the external electric field and the built-in electric field due to the polarization are co-directed, leading to a poorer emission wavelength stability upon the bias variation.

4.2.2. Structure with graded-composition emitters

This heterostructure (see Table 4 for detailed description) has a linearly graded composition of the n-contact layer (varied from GaN to $Ga_{0.92}In_{0.08}N$) next to the $Ga_{0.8}In_{0.2}N$-SQW and a linearly graded composition of the p-AlGaN emitter (from $Al_{0.05}Ga_{0.95}N$ to $Al_{0.2}Ga_{0.8}N$). The graded-composition layers provide a distributed polarization doping in the LED structure [9], on the one hand, and built-in fields pulling electrons and holes, on the other hand.

The band diagram, carrier distributions and recombination rates at low and high values of the current density in the structure are shown in Fig. 7. Employing of the graded-composition GaInN emitter beneath the GaInN quantum well allows to lower the potential barrier to electrons at the n-emitter/QW interface at a high injection level. Similarly, the graded-composition AlGaN lowers such a barrier to holes at the quantum well/p-emitter interface. In addition, the carrier confinement near the SQW is improved compared to the LED structure with constant composition of the layers.

In contrast to the structures with the constant layer composition, the ionized donor concentrations in the graded-composition heterostructure is found to depend on bias in the graded GaInN layer. The radiative recombination is well located in the quantum well, while the non-radiative carrier recombination occurs mainly in the graded GaInN layer (Figs. 7(e) and (f)) at a low injection level and has pronounced tails in the layers adjacent to the SQW at a high injection level.

The emission spectra of the SQW LED considered in the preceding section (a) and of the graded-composition LED (b) are shown in Fig. 8. It can be seen that there is no remarkable difference in the spectra behavior with current. At a high injection level, a blue shift of the spectrum and its broadening is observed in both heterostructures, which is related to the contribution of second confined state of electrons in the quantum well. The spectral peak predicted for the LED with the constant layer composition is in a fair agreement with the data (2.77–2.80 eV) obtained in [27] in different samples. Fig. 9 compares the emission peak position as a function of current density measured in [27] and calculated for the InGaN SQW structure with the InN molar fraction $x = 0.215$. Fair agreement between the theory and experiment is seen from the figure.

The IQEs versus current density computed for these two LED structures are plotted in Fig. 10. It is seen that the graded-composition LED exhibits a lower emission efficiency at the low current densities. It is also found that the graded-composition LED provides a higher turn-on voltage. From this point of view, this particular graded-composition LED structure has a poorer performance compared to the structure with constant layer composition. Nevertheless, we believe that the potential of graded-composition layers is not yet realized in full measure. As the use of such layers provides additional degree of freedom for bandgap engineering of LED structures, more efforts are required to recognize and utilize the new opportunity.

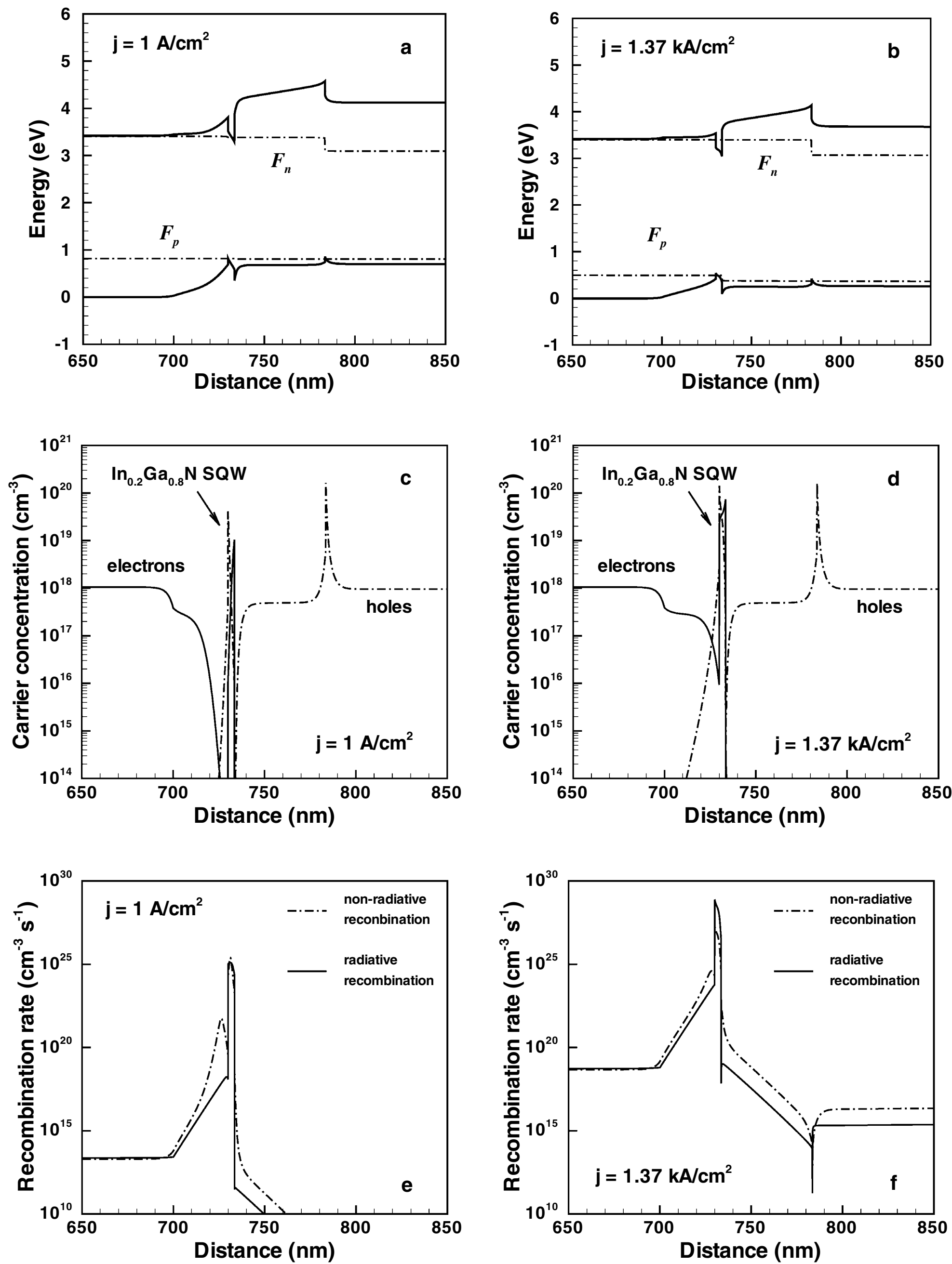

Fig. 7. Graded-composition SQW LED structure at $j = 1$ A/cm^2 (left) and 1.37 kA/cm^2 (right): (a), (b) band diagram; (c), (d) carrier concentration; (e), (f) recombination rates.

4.3. UV multiple-quantum well LED

Development of UV LEDs is an important field of modern optoelectronic industry. Such devices are normally based on In-free heterostructures with the active region made either of GaN (emission wavelength about 365 nm) or AlGaN (emission wavelength down to 250 nm). The use in these devices of AlGaN with high AlN content creates additional problems related, first of all, to extremely low acceptor

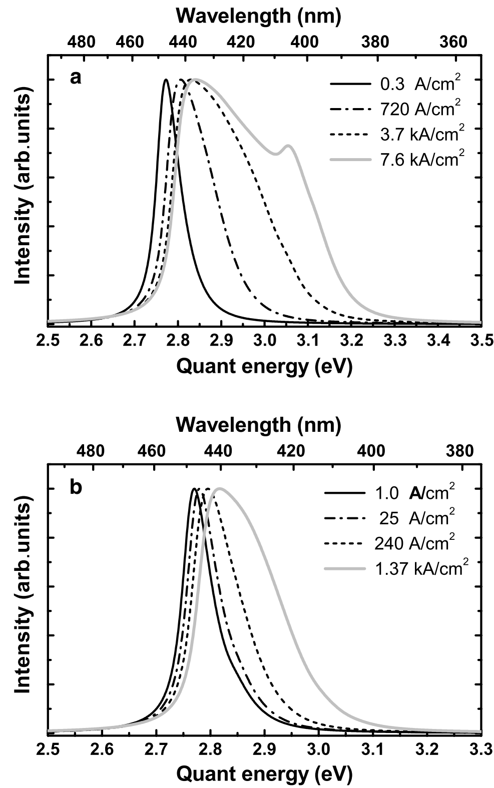

Fig. 8. Emission spectra of SQW LED structures with constant layer composition (a) and graded-composition emitters (b).

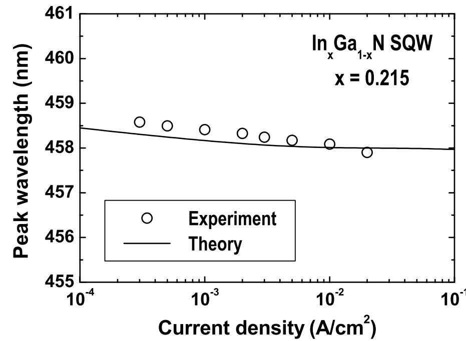

Fig. 9. Peak wavelength shift with the current density in InGaN SQW LED structure with constant layer composition: comparison of theoretical predictions with experiment.

activation efficiency, poor electron and hole confinement, and poor ohmic contacts to both n- and p-type layers. Therefore, development of UV LED heterostructures requires especially careful design.

In this subsection, we will demonstrate applicability of our model to analysis of a UV LED operation. As an example, the LED structure reported in [85] has been chosen for simulations. The parameters of the multiple-quantum-well (MQW) heterostructure are given in Table 5. The Ga(Al)-polarity of the whole structure is assumed in the computations and the threading dislocation density of 10^{10} cm^{-2} is taken in accordance with observation that the MOCVD-grown AlGaN epilayers with high AlN content, exhibit normally a higher defect level. At such dislocation density, the non-radiative life times of electrons and holes are 0.08 and 0.3 ns,

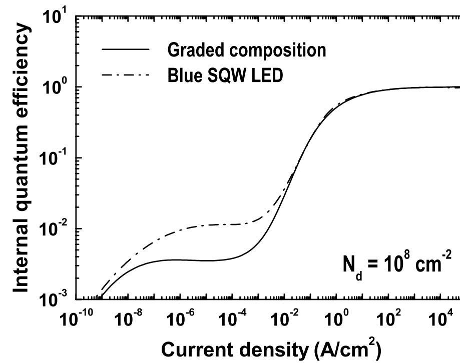

Fig. 10. IQEs of SQW LED structures with constant layer composition and graded-composition emitters.

Table 5
MQW UV LED structure

Layer	Thickness (nm)	Material	Type	Doping (cm^{-3})
n-Contact	700	$Al_{0.48}Ga_{0.52}N$	n	2×10^{19}
QW	2	$Al_{0.36}Ga_{0.64}N$	UID	–
Barrier	5	$Al_{0.48}Ga_{0.52}N$	n	2×10^{19}
QW	2	$Al_{0.36}Ga_{0.64}N$	UID	–
Barrier	5	$Al_{0.48}Ga_{0.52}N$	n	2×10^{19}
QW	2	$Al_{0.36}Ga_{0.64}N$	UID	–
p-Emitter	10	$Al_{0.6}Ga_{0.4}N$	p	7×10^{19}
p-Contact	500	GaN	p	7×10^{19}

respectively. In the simulations, we also use the acceptor activation energy of 350 meV to account for a lower acceptor activation efficiency in AlGaN with high AlN content.

Some results of he LED structure simulation are presented in Fig. 11. The band diagram (Fig. 11(a)) is found to be quite stable upon the current density variation. The carrier concentrations (Fig. 11(c)) exhibit a non-uniform filling of individual QWs, which is especially pronounced for holes having much lower mobility. As a result, the carrier recombination occurs mainly in the QW adjacent to the p-AlGaN emitter (Fig. 11(d)). The electric field in the QWs is smaller compared to the InGaN LEDs due to a lower polarization charges on the MQW interfaces (Fig. 11(b)).

The computed emission spectrum is plotted in Fig. 12. Detailed analysis of the electronic states in the QWs shows that the splitting and broadening of the spectrum is related to the appearance of the extra electron two-dimensional subband at a high bias. The computed peak wavelength agrees well with that measured in [85].

The data reported in [85] allow calculation of the external emission efficiency of the UV LED as a function of current density in a wide range of its variation. We have found a close correlation between the predicted IQE and the measured external efficiency as shown in Fig. 13. The deviations observed at low current densities is apparently related to non-ohmic contact to n- and especially p-layers. Another discrepancy observed at a high current densities has presumably the same nature as that in the InGaN QW heterostructures, which requires further studies to be understood.

The above modelling results clearly show the importance of the dislocation density for the LED performance. Actually, the dislocation density is the most critical parameter controlling the IQE of group-III nitride LEDs. A higher effective dislocation density in the In-free heterostructures is one of the reasons why the UV LEDs normally exhibit much poorer efficiency than the InGaN blue and even green LEDs. Other aspects of MQW LED operation, including selective barrier doping, are discussed in detail in [86].

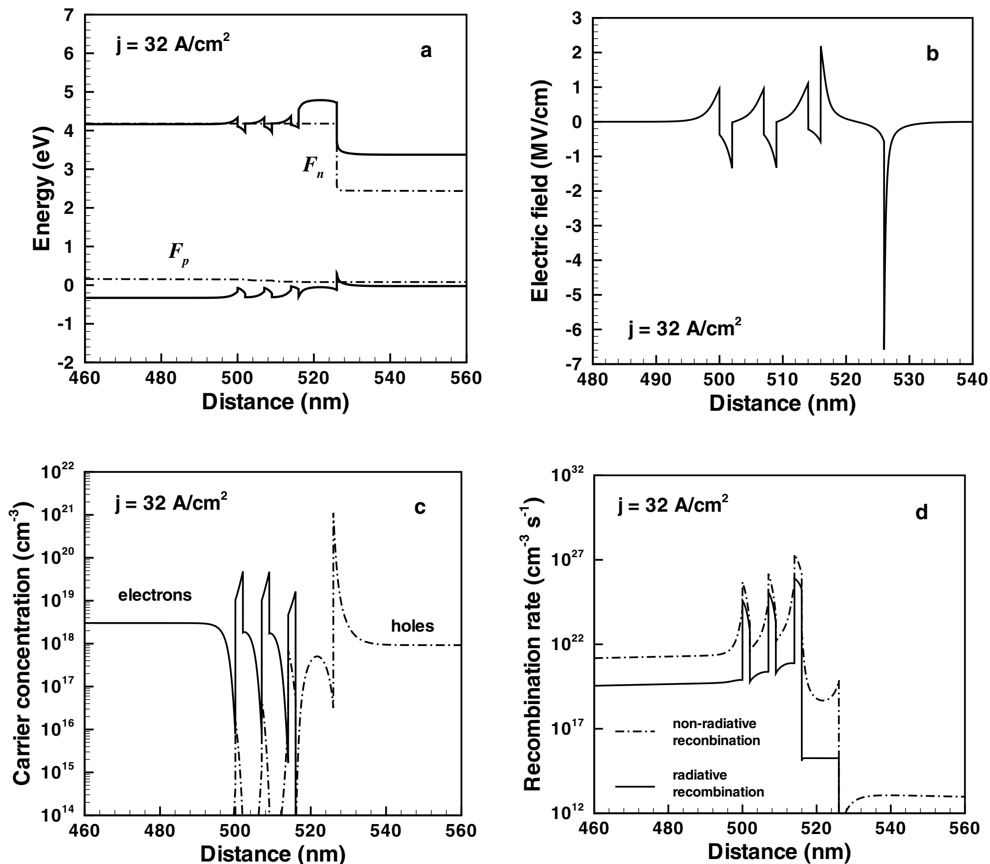

Fig. 11. MQW UV LED structure at $j = 32$ A/cm^2: (a) band diagram; (b) electric field; (c) carrier concentration; (d) recombination rates.

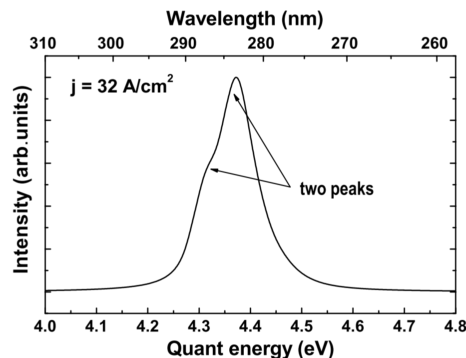

Fig. 12. MQW UV LED structure: emission spectrum at $j = 32$ A/cm^2.

5. Summary

We have examined the applicability of a one-dimensional DD model to simulation of the carrier transport and light emission in III-nitride LED heterostructures. The numerical implementation of the model based on the mixed finite-element approach is found to be most appropriate for modelling of the wide-bandgap devices. Despite the inherent inaccuracy of the DD approach that ignores the carrier delocalization due to quantum-size effects, the DD model is found to reproduce basic trends in the III-nitride LED operation, like the spontaneous

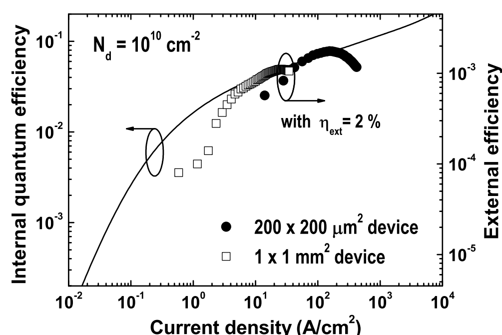

Fig. 13. MQW UV LED structure: correlation between internal and external quantum efficiency as a function of current density.

and piezo-polarization impact on the band diagram and the IQE dependence on the threading dislocation density in epitaxial materials. The former allows, in particular, a better understanding of the role of crystal polarity in bandgap engineering of LED heterostructures. The latter provides a tool for the structure optimization aimed at increasing of the LED IQE. Potential of distributed polarization doping in graded-composition III-nitride materials for designing of LED structures is, in our opinion, still underestimated. However, because of the competition between the enhanced carrier concentration and built-in pulling field, the advantages of the graded-composition alloys can be utilized in full measure only on the basis of a careful examination of their total effect on the device performance. For this, numerical simulation may be especially helpful.

We have found that the computations of the light emission spectra based on the quantum-mechanical treatment of carriers confined in the QW active regions of LEDs provide quite reasonable predictions for the peak wavelength position and its shift with current through the diode. The predictability of the model can be further improved by accounting for the strain-dependent valence subband shifts which are expected to affect not only the material bandgap but also the conduction and valence band offsets at the QW interfaces. Alternative radiative recombination channels like those involving holes bound by deep Mg acceptors should be considered additionally in the structures with doped/co-doped active region.

Our simulations have revealed that the theoretical *I–V* characteristics of III-nitride LEDs are inadequate at low-current operation, which is because of neglecting the tunnelling current. As the latter is essentially nonlocal, a special approach for modelling the tunnelling current has to be developed, compatible with the local DD model, or hybrid simulations with a smart separation and coupling of the classical and quantum regions should be applied.

In this paper, we have considered by modelling various III-nitride SQW and MQW LED heterostructures operating in both visible and UV spectral ranges. The comparison of simulations with available data justifies that the DD model employed in this study could generally serve as an effective tool for the LED design and optimization.

Acknowledgments

The authors are grateful to K.L. Safonov and A.V. Tsyryulnikov for the development of the graphic user interface for the SiLENSe code, to N.I. Podolskaya for the help with the database of nitride material properties.

References

[1] J.W. Orton, C.T. Foxon, Group III nitride semiconductors for short wavelength light emitting devices, Rep. Prog. Phys. 61 (1998) 1.
[2] O. Ambacher, Growth and applications of group III-nitrides, J. Phys. D 31 (1998) 2653.
[3] X. Guo, E.F. Schubert, Current crowding and optical saturation effect in GaInN/GaN light emitting diodes grown on insulating substrates, Appl. Phys. Lett. 78 (2001) 3337.
[4] N. Narendran, Y. Gu, J.P. Freyssinier, H. Yu, L. Deng, Solid-state lighting: failure analysis of white LEDs, J. Cryst. Growth 268 (2004) 449.

[5] P. Shah, V. Mitin, M. Grupen, H. Song, K. Hess, Numerical simulation of wide band-gap AlGaN/InGaN light emitting diodes for output power characteristics and emission spectra, J. Appl. Phys. 79 (1996) 2755.
[6] S. Nakamura, T. Mukai, M. Senoh, Candela-class high-brightness InGaN/AlGaN double-heterostructure blue-light emitting diodes, Appl. Phys. Lett. 64 (1994) 1687.
[7] M. Hansen, J. Piprek, P.M. Pattison, J.S. Speck, S. Nakamura, S.P. DenBaars, Higher efficiency InGaN laser diodes with an improved quantum well capping configuration, Appl. Phys. Lett. 81 (2002) 4275.
[8] J. Piprek, Simulation of GaN-based light emitting devices, in: G. Wachutka, G. Schrag (Eds.), Simulation of Semiconductor Processes and Devices, Springer, Wien, 2004.
[9] D. Jena, S. Heikman, J.S. Speck, U.K. Mishra, A. Link, O. Ambacher, Magnetotransport measurement of effective mass, quantum scattering time, and alloy scattering potential of polarization-doped 3D electron slabs in graded-AlGaN, Phys. Stat. Solidi (c) O (2003) 2339.
[10] S.Y. Karpov, Y.N. Makarov, Dislocation effect on light emission efficiency in gallium nitride, Appl. Phys. Lett. 81 (2002) 4721.
[11] A.E. Yunovich, V.E. Kudryashov, A.N. Turkin, A. Kovalev, F. Manyakhin, The emission properties of light emitting diodes using InGaN/AlGaN/GaN multiple quantum wells, MRS J. Nitride Semicond. Res. 3 (1998) 44.
[12] J.F. Nye, Physical properties of crystals, The Representation by Tensors and Martices, Clarendon Press, Oxford, 1964.
[13] D. Xiao, K.W. Kim, S.M. Bedair, J.M. Zavada, Design of white light emitting diodes using InGaN/AlInGaN quantum-well structures, Appl. Phys. Lett. 84 (2004) 672.
[14] B. Monemar, G. Pozina, Group III-nitride based hetero and quantum structures, Prog. Quantum Electron. 24 (2000) 239.
[15] D. Vasileska, S.M. Goodnick, Computational electronics, Mater. Sci. Eng. R 38 (2002) 181.
[16] M.V. Fischetti, S.E. Laux, Monte-Carlo analysis of electron transport in small semiconductor devices including band-structure and space-charge effects, Phys. Rev. 38 (1988) 9721.
[17] M. Saraniti, J. Tang, S.M. Goodnick, S.J. Wigger, Numerical challenges in particle-based approaches for the simulation of semiconductor devices, Math. Comput. Simul. 62 (2003) 501.
[18] P. Degond, C. Schmeiser, Macroscopic models for semiconductor heterostructures, J. Math. Phys. 39 (1998) 4634.
[19] A. Jüngel, Quasi-Hydrodynamic Semiconductor Equations, Birkhäuser-Verlag, 2000.
[20] A. El Ayyadi, A. Jüngel, Semiconductor simulations using a coupled quantum drift-diffusion Schrödinger–Poisson model, der Johannes Gutenberg-Universität, Mainz, 2004, p. 1 (preprint 09/04).
[21] J.A. Carrillo, I.M. Gamba, O. Muscato, C-W. Shu, Comparison of Monte Carlo and deterministic simulations of a silicon diode, Universitá degli Studi di Catania, 2000, p. 1 (preprint).
[22] S.M. Sze, Physics of Semiconductor Devices, Wiley, New York, 1981.
[23] N. Ben Abdallah, M.L. Tayer, Diffusion approximation for the one dimensional Boltzmann–Poisson system, Discrete Cont. Dyn. Syst. B 4 (2004) 1129.
[24] W. Van Roosbroeck, Theory of flow of electrons and holes in germanium and other semiconductors, Bell Syst. Tech. J. 29 (1950) 560.
[25] V. Palankovski, R. Quay, S. Selberherr, Industrial application of heterostructure device simulation, IEEE J. Solid-State Circuits 36 (2001) 1365.
[26] X.A. Cao, J.M. Teetsov, F. Shahedipour-Sandvik, S.D. Arthur, Microstructural origin of leakage current in GaN/InGaN light emitting diodes, J. Cryst. Growth 264 (2004) 172.
[27] K.G. Zolina, V.E. Kudryashov, A.N. Turkin, A.E. Yunovich, S. Nakamura, Luminescence spectra of superbright blue and green InGaN/AlGaN/GaN light emitting diodes, MRS J. Nitride Semicond. Res. 1 (1996) 11.
[28] X.A. Cao, K. Topol, F. Shahedipour-Sandvik, J.M. Teetsov, P.M. Sandvik, S.F. LeBoeuf, et al., Influence of defects on electrical and optical characteristics of GaN/InGaN-based light emitting diodes, GE Global Research, Technical Report 2002GRC206, 2002, p. 1.
[29] X.A. Cao, J.M. Teetsov, M.P. D'Evelyn, D.W. Merfeld, Electrical characteristics of InGaN/GaN light emitting diodes grown on GaN and sapphire substrates, Appl. Phys. Lett. 85 (2004) 7.
[30] S.L. Chuang, C.S. Chang, $\mathbf{k} \times \mathbf{p}$ method for strained wurtzite semiconductors, Phys. Rev. B 54 (1996) 2491.
[31] E.P. Doolan, J.J.H. Miller, W.H.A. Shielders, Uniform Numerical Methods for Problems with Initial and Boundary Layer, Boole, Dublin, 1980.
[32] J.J.H. Miller, W.H.A. Shielders, S. Wang, Application of finite element methods to the simulation of semiconductor devices, Rep. Prog. Phys. 62 (1999) 277.
[33] R.E. Bank, D.J. Rose, W. Fichtner, Numerical methods for semiconductor device simulation, IEEE Trans. Electron. Dev. 30 (1983) 1031.
[34] M.S. Mock, On equations describing steady state carrier distribution in a semiconductor device, Commun. Pure Appl. Math. 25 (1972) 781.
[35] P.A. Markowich, A singular perturbation analysis of the fundamental semiconductor device equations, SIAM J. Appl. Math. 5 (1984) 896.
[36] J.W. Jerome, T. Kerkhoven, A finite element approximation theory for the drift-diffusion semiconductor model, SIAM J. Numer. Anal. 28 (1991) 403.
[37] J.W. Jerome, The mathematical study and approximation of semiconductor models, in: Gilbert, Kershaw (Eds.), Large Scale Matrix Problems and the Numerical Solution of Partial Differential Equations, Oxford University Press, Oxford, 1994, p. 157.
[38] F. Alabau, Structural properties of the one-dimensional drift-diffusion models for semiconductors, Trans. Am. Math. Soc. 348 (1996) 823.
[39] S.J. Polak, C. Den Heijer, W.H.A. Schilders, P.A. Markowich, Semiconductor device modelling from the numerical point of view, Int. J. Numer. Math. Eng. 24 (1987) 763.

[40] J.W. Slotboom, Iterative scheme for 1- and 2-dimensional D.C. transistor simulation, Electron. Lett. 5 (1969) 677.
[41] D.N. Allen, R.V. Southwell, Relaxation methods applied to determine the motion in 2-D of a viscous fluid past a fixed cylinder, Quart. J. Mech. Appl. Math. VIII (1955) 129.
[42] A.M. Il'in, Differencing scheme for a differential equation with a small parameter affecting the highest derivative, Math. Notes 6 (1969) 596.
[43] D.L. Scharfetter, H.K. Gummel, Large signal analysis of a Silicon Read diode oscillator, IEEE Trans. Electron. Dev. 16 (1969) 64.
[44] K.-J. Bathe, Finite Element Procedures, Prentice-Hall, Englewood Cliffs, NJ, 1996.
[45] R.E. Bank, D. Rose, Parameter selection for Newton-like methods applicable to nonlinear partial differential equations, SIAM J. Numer. Anal. 17 (1980) 806.
[46] J.M. Ortega, W.C. Rheinbolt, Iterative Solution of Nonlinear Equations of Several Variables, Academic Press, New York, 1970.
[47] H.K. Gummel, A self-consistent iterative scheme for one-dimensional steady state transistor computation, IEEE Trans. Electron. Dev. 11 (1964) 455.
[48] S. Micheletti, A. Quarteroni, R. Sacco, Current–voltage characteristics simulation of semiconductor devices using domain decomposition, J. Comput. Phys. 119 (1995) 46.
[49] Q.E. Akcasu, Convergence properties of Newton's method for the solution of the semiconductor transport equations and hybrid solution techniques for multidimensional simulation of VLSI devices, Solid-State Electron. 27 (1984) 319.
[50] A. Boukili, A. Marrocco, Arclength continuation methods and applications to 2D drift-diffusion semiconductor equations, Report No2546 of Institut National de Recherche en Informatique et Automatique, 1995, p. 1.
[51] E.L. Allgower, K. Georg, Numerical path following, in: P.G. Ciarlet, J.L. Lions (Eds.), Techniques of Scientific Computing (Part 2), Handbook of Numerical Analysis, vol. 5, North-Holland, Amsterdam, 1997, p. 3.
[52] Available from: <http://www.semitech.us/products/SiLENSe/>.
[53] P.J. Roache, Verification and Validation in Computational Science and Engineering, Hermosa Publishers, Albuquerque, NM, 1998.
[54] W.L. Oberkampf, T.G. Trucano, Verification and validation in computational fluid dynamics, Prog. Aerospace Sci. 38 (2002) 209.
[55] L. Hatton, The T experiments: errors in scientific software, IEEE Comput. Sci. Eng. 4 (1977) 27.
[56] S.-H. Chou, Q. Li, Error estimates in L^2, H^1 and L^∞ in covolume methods for elliptic and parabolic problems: a unified approach, Math. Comp. 69 (2000) 103.
[57] H. Kim, S.-J. Park, H. Hwang, Effects of current spreading on the performance of GaN-based light emitting diodes, IEEE Trans. Electron. Dev. 48 (2001) 1065.
[58] A. Kaneta, T. Izumi, K. Okamoto, Y. Kawakami, S. Fuita, Y. Narita, et al., Spatial inhomogeneity of photoluminescence in an InGaN-based light emitting diode structure probed by near-field microscopy under illumination-collection mode, Jpn. J. Appl. Phys. 40 (2001) 110.
[59] S. Nakamura, InGaN/AlGaN blue-light emitting diodes, J. Vac. Sci. Technol. A 13 (1995) 705.
[60] J. Wu, W. Walukiewicz, Band gaps of InN and group III nitride alloys, Superlattices Microstruct. 34 (2003) 63.
[61] V. Fiorentini, F. Bernardini, O. Ambacher, Evidence for nonlinear polarization in III–V nitride alloy heterostructure, Appl. Phys. Lett. 80 (2002) 1204.
[62] M. Farahmand, C. Garetto, E. Bellotti, K.F. Brennan, M. Goano, E. Ghillino, et al., Monte Carlo simulation of electron transport in the III-nitride wurzite phase materials system: binaries and ternaries, IEEE Trans. Electron. Dev. 48 (2001) 535.
[63] A.F.M. Anwar, S. Wu, R.T. Webster, Temperature dependent transport properties in GaN, $Al_xGa_{1-x}N$ and $In_xGa_{1-x}N$ semiconductors, IEEE Trans. Electron. Dev. 48 (2001) 567.
[64] S. Stepanov, W.N. Wang, B.S. Yavich, V. Bougrov, Y.T. Rebane, Y. Shreter, Influence of Poisson's ratio uncertainty on calculations of the bowing parameter for strained inGaN layers, MRS J. Nitride Semicond. Res. 6 (2001) 6.
[65] H. Angerer, D. Brunner, F. Freudenberg, O. Ambacher, M. Stutzman, R. Hopler, et al., Determination of the Al mole fraction and bandgap bowing of epitaxial AlGaN films, Appl. Phys. Lett. 71 (1997) 1504.
[66] O. Katz, B. Meyler, U. Tisch, J. Salzman, Determination of band-gap bowing for $Al_xGa_{1-x}N$ alloys, Phys. Stat. Sol. (a) 188 (2001) 789.
[67] F. Yun, M.H. Reshchikov, L. He, T. King, H. Morkoc, S.W. Novak, et al., Energy band bowing parameter in $Al_xGa_{1-x}N$ alloys, J. Appl. Phys. 92 (2002) 4837.
[68] K.S. Kim, A. Saxler, P. Kung, M. Razeghi, K.Y. Lim, Determination of the band-gap energy of AlInN grown by metal-organic chemical-vapor deposition, Appl. Phys. Lett. 71 (1997) 800.
[69] I. Akasaki, H. Amano, Crystal growth and conductivity control of group III nitride semiconductors and their application to short wavelength light emitters, Jpn. J. Appl. Phys. 36 (1997) 5393.
[70] M. Leszcynski, T. Suski, H. Teisseyre, P. Perlin, I. Grzegory, J. Jun, et al., Thermal expansion of gallium nitride, J. Appl. Phys. 76 (1994) 4909.
[71] M. van Schilfgaarde, A. Sher, A.-B. Chen, Theory of AlN, GaN, InN and their alloys, J. Cryst. Growth 178 (1997) 8.
[72] S.N. Mohammad, H. Morkoc, Progress and prospects of group-III nitride semiconductors, Prog. Quantum Electron. 20 (1996) 361.
[73] D. Cherns, J. Barnard, F.A. Ponce, Measurement of the piezoelectric field across strained InGaN/GhaN layers by electron holography, Solid-State Commun. 111 (1999) 281.
[74] V.W.L. Chin, T.L. Tansley, T. Osotchan, Electron mobilities in gallium, indium, and aluminum nitrides, J. Appl. Phys. 75 (1994) 7365.
[75] M.E. Levinshtein, S.L. Rumyantsev, M.S. Shur (Eds.), Properties of Advanced Semiconductor Materials. GaN, AlN, InN, BN, SiC, SiGe, Wiley–Interscience, New York, 2001.
[76] Available from: <www.iiiv.cornell.edu/www/foutz/nitride.html>.

[77] D.J. Dugdale, S. Brandt, R.A. Abram, Direct calculations of $\boldsymbol{k} \times \boldsymbol{p}$ parameters for wurtzite AlN, GaN, and InN, Phys. Rev. B 61 (2000) 12933.
[78] T.-H. Yu, K.F. Brennan, Theoretical study of the two-dimensional electron mobility in strained III-nitride heterostructures, J. Appl. Phys. 89 (2001) 3827.
[79] J.S. Im, A. Moritz, F. Steuber, V. Hařle, F. Scholz, A. Hangleiter, Radiative carrier lifetime, momentum matrix element, and hole effective mass in GaN, Appl. Phys. Lett. 70 (1997) 631.
[80] S. Nakamura, InGaN-based violet laser diodes, Semicond. Sci. Technol. 14 (1999) R27.
[81] R.F. Kazarinov, M.R. Pinto, Carrier transport in laser heterostructures, IEEE J. Quantum Electron. QE-30 (1994) 49.
[82] C.C. Pan, C.M. Lee, J.W. Liu, G.T. Chen, J.I. Chyi, Luminescence efficiency of InGaN multiple-quantum-well ultraviolet light emitting diodes, Appl. Phys. Lett. 84 (2004) 5249.
[83] F. Manyukhin, A. Kovalev, A.E. Yunovich, Aging mechanisms of InGaN/AlGaN/GaN light emitting diodes operating at high currents, MRS J. Nitride Semicond. Res. 3 (1998) 53.
[84] S.Yu. Karpov, K.A. Bulashevich, I.A. Zhmakin, M.O. Nestoklon, V.F. Mymrin, Yu.N. Makarov, Carrier injection and light emission in visible and UV nitride LEDs by modeling, Phys. Stat. Sol. (a) 241 (2004) 668.
[85] A.J. Fischer, A.A. Allerman, M.H. Crawford, K.H.A. Bogart, S.R. Lee, R.J. Kaplar, W.W. Chow, S.R. Kurtz, K.W. Fullmer, J.J. Figiel, Room-temperature direct current operation of 290 nm light emitting diodes with milliwatt power levels, Appl. Phys. Lett. 84 (2004) 3394.
[86] V.F. Mymrin, K.A. Bulashevich, N.I. Podolskaya, I.A. Zhmakin, S.Yu. Karpov, Yu.N. Makarov, Modelling of MQW LED operation, Phys. Stat. Sol. (c) 2 (2005) 2928.